



Modeling landslide activity and sediment connectivity after eruptions: Insights from the Blanco River (Chile)

Alberto Paredes^a, Lorenzo Martini^{b,*}, Andrés Iroumé^c, Lorenzo Picco^b

^a Universidad Austral de Chile, Graduate School, Doctorate in Forest Sciences and Natural Resources, Faculty of Forest Sciences and Natural Resources, Valdivia, Chile

^b University of Padova, Department of Land, Environment, Agriculture and Forestry, Legnaro, Italy

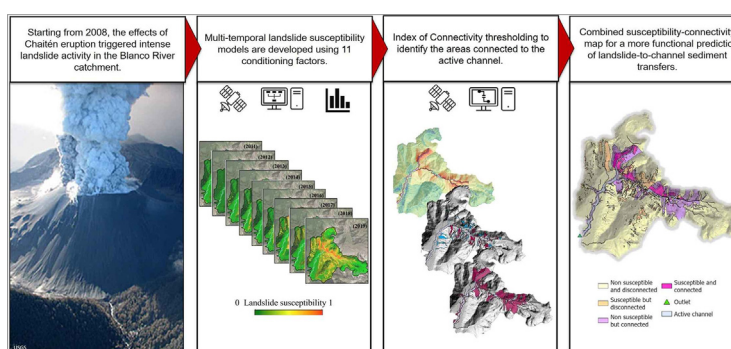
^c Universidad Austral de Chile, Faculty of Forest Sciences and Natural Resources, Valdivia, Chile



HIGHLIGHTS

- Changes in landslide susceptibility were assessed in a volcano-affected catchment.
- A threshold-based connectivity map is derived using logistic regressions.
- Fast re-vegetation affects the accuracy of landslide susceptibility models.
- Areas susceptible and connected represent 3.1 % of the Blanco River catchment.
- Joint susceptibility-connectivity map helps predict sediment supply from hillslopes.

GRAPHICAL ABSTRACT



ARTICLE INFO

Editor: Paulo Pereira

Keywords:

Landslides
Connectivity
Volcanic eruption
Chile
Forest cover changes

ABSTRACT

Volcanic eruptions can disrupt entire river basins by affecting the hydro-geomorphic characteristics of channel networks and hillslopes. Reports suggest a pulsed and delayed increase in landslide activity following the eruptions, which, depending on the degree of linkage between hillslopes and channels, i.e. sediment connectivity, can represent a massive source of sediment input for the fluvial system. Therefore, predicting landslide occurrence and sediment connectivity is fundamental for management risk strategies, especially in such dynamic and complex environments. The aim of this work is to develop and offer a more reliable approach to map the areas susceptible to landslides and connected to the active channel in a catchment impacted by volcanic eruption. The analyses were carried out in the Blanco River catchment in southern Chile, affected by the Chaitén eruption (2008–09). A combined approach is presented, based on landslide susceptibility models, carried out multi-temporally (from 2010 to 2019), and a threshold-based sediment connectivity map. The results showed that the highest landslide occurrence was reported 4 years after the eruption, whereas the faster increase in the overall area affected was observed only after 7 years. Landslide susceptibility models showed high accuracy when applied in the same year, but were less accurate in predicting future occurrences. This result is ascribed to the dynamic conditions of the vegetation, regenerating quickly after the mass movements. Nevertheless, considering the potential sources of error, the combined landslide susceptibility-connectivity map for the year 2019 well-identified relevant areas for catchment management. The largest part of the catchment was found non-susceptible and disconnected, while areas classified as susceptible and connected represent only 3.1 %. The application of this novel approach allowed to unravel the geomorphic trajectory of the study area and, more importantly, can represent a benchmark for future applications in other catchments affected by large disturbances.

* Corresponding author at: viale dell'Università 16, Legnaro, PD 35020, Italy.
E-mail address: lorenzo.martini@unipd.it (L. Martini).

1. Introduction

The morphology of river systems is in constant dynamism due to changes in the balance between water and sediments (Sulaiman et al., 2021). Their transport dynamics rapidly adjust thanks to multiple factors acting on different temporal and spatial scales (Batalla et al., 2018; Brasington et al., 2012). In particular, river morphology is transformed by alternations of sedimentation and erosion processes within the channel, in the floodplain, and by changes in the surrounding hillslopes (Rathburn et al., 2017; Ulloa et al., 2018). These processes can be altered by anthropogenic disturbances, such as gravel mining, dams and change in land use (Picco et al., 2017; Sanchis-Ibor et al., 2017; Villablanca et al., 2022). Furthermore, river systems can be disrupted by large natural disturbances, such as tectonic activity, glacier volume fluctuations, volcanic eruptions, extreme floods, mass movements along the slopes (Iroumé et al., 2020; Pellegrini et al., 2021; Wang et al., 2017; Wasko et al., 2020; Wilson et al., 2019; Zanandrea et al., 2020). Among these disturbances, volcanic eruptions generate major changes in rivers, affecting the hydrological and sedimentary dynamics, the storage and transport of woody debris, and consequently producing a wide range of hazards for nearby settlements (Somos-Valenzuela et al., 2020; Ulloa et al., 2016). In particular, pyroclastic flows and tephra falls can cover large areas with primary volcanoclastic particles (Alfano et al., 2011), affecting vegetation cover, decreasing leaf interception capacity, and evapotranspiration (Crisafulli et al., 2015). The accumulation of tephra and vegetation mortality gradually enhance the instability of the slopes due to the loss of root strength as a result of their decomposition (Major et al., 2018). As consequence, increased sediment fluxes from the slopes into the channel network are expected (Clapuyt et al., 2019).

There is evidence that the secondary effects of volcanic eruptions, especially in areas affected by severe tephra falls, involve an increase in pulsed and delayed landslide activity (between 4 and 8 years after the disturbance) (Korup et al., 2019). In forested watersheds, the main sediment and LW inputs are from adjacent hillslopes and lateral erosion of the channels (Hassan et al., 2019). On slopes coupled to the active channel, landslides can provide large sediment inputs, whereas, on uncoupled slopes, lateral sediment inputs are hindered by landform buffers, like broad alluvial plains, reducing overall the degree of connectivity (Fryirs, 2013). Sediment connectivity is a well-known property of any geomorphic system (Wohl et al., 2018) and it describes the capacity of the sediment to follow a transfer path and reach a determined sink area (Hooke, 2003; Bracken et al., 2015). Therefore, in post-disturbance scenarios, assessing the degree of connectivity means understanding if lateral sediment inputs can affect the drainage pattern, potentially causing accelerated adjustments and changing the structure and shape of river systems (Martini et al., 2019; Ortíz-Rodríguez et al., 2017; Poepl et al., 2020; Schopper et al., 2019).

Several studies have shown how the configuration of local geo-environmental conditions (topography, lithology, and vegetation) in conjunction with the interaction of external triggers (e.g. earthquakes, extreme rainfall events) determine the probability of landslides occurrence (Arabameri et al., 2019; Guzzetti et al., 2012; Reichenbach et al., 2018). However, due to the vast diversity of geo-environmental settings prone to landslide occurrence, the development of reliable spatial landslide susceptibility maps remains a challenge. For this reason, landslide susceptibility models should be carried out in different environments under various geo-environmental settings (Gariano and Guzzetti, 2016; Guzzetti et al., 2012, 1999; Lai and Tsai, 2019; Yi et al., 2020). Recently, studies oriented to landslide susceptibility through machine learning, deep learning algorithms, and non-temporal landslide inventory have been carried out in volcanic environments in the northern Chilean Patagonia, where the authors focused on the conditioning and triggering factors of this region (Lizama et al., 2022; Morales et al., 2022; Morales et al., 2021; Parra et al., 2021). However, less information is available on how the conditioning factors mutate over time and how this could affect landslide occurrence temporally, other than spatially.

Even less investigated is the relationship between landslide susceptibility and connectivity. As previously mentioned, the degree of connectivity regulates the proportion of sediment reaching a specific area of a catchment (Heckmann et al., 2018). However, its assessment is often carried out with semi-quantitative maps (Cavalli et al., 2013) without proper validations. Recent advances in the field of sediment connectivity proposed the quantification of connectivity thresholds to characterize at what degree the sediment can really be conveyed from sources to channels in mountain catchments (Abatti et al., 2022; Martini et al., 2022a; Spiekermann et al., 2022a; Steger et al., 2022). Moving toward the combination of susceptibility maps and threshold-based connectivity maps is fundamental to achieving a deeper and more quantitative understanding of sediment transfer dynamics in mountain catchments, especially if affected by large natural disturbances.

In this study, the main aim is to develop and offer a reliable approach to map the areas susceptible to landslides and, at the same time, connected to the active channel in a catchment impacted by a volcanic eruption. In this perspective, it would be possible to predict and prioritize only the areas that are expected to convey large amounts of sediment downstream, causing potential hazardous consequences. Secondary objectives are to: i) investigate how volcanic eruptions affect the temporal variation of landslide occurrence and susceptibility in a catchment, and ii) understand how and why the conditioning factors of landslide susceptibility evolve within a time window of 9 years. Fulfilling the objectives would greatly improve the understanding of landslide dynamics in this environment but, more importantly, it would provide a workflow to be tested and applied in other areas affected by other large disturbances, where managing sediment transfers from hillslope is the first priority.

2. Study area

The Blanco River flows in southern Chile, draining the southern slope of the Chaitén volcano (72°39'7"W, 42°50'1"S) (Fig. 1). The basin area is 73 km² with altitudes between 0 and 1545 m a.s.l. The catchment drains from the caldera of the Chaitén volcano, which contribute to the main channel thanks to the Caldera Creek, and from the south-western slopes connected to the Michinmahuida volcano. The annual precipitation in the surrounding area ranges from 2500 to 5000 mm (Dirección Meteorológica de Chile, <https://climatologia.meteochile.gob.cl/>; 2023), hence the Blanco River has a rain-dominated regime with maximum discharges in the winter season. The main valley is glacially incised on a tectonic lineament (Iroumé et al., 2020) and the slopes average between 35° - 45°, with maximum peaks reaching up to 70°. The soils are mostly andosols and histosols placed on granodiorite and greenschist bedrock (Casanova et al., 2013; Pierson et al., 2013); they are quite unstable, thus favoring sliding phenomena. Alluvial deposits are present in low-lying areas where they are interspersed with pyroclastic deposits (Ulloa et al., 2016). The forest corresponds to the evergreen forest type (Swanson et al., 2013), characterized by high species diversity and the presence of *Nothofagus dombeyi*, *N. nitida*, *N. betuloides*, *Luma apiculata*, *Drimys winteri*, *Eucryphia cordifolia*, *Weinmannia trichosperma*, and *Aextoxicon punctatum*. The understorey is dominated by *Gunnera tinctoria*, a fast-growing endemic species with large leaves. The study was carried out in the Blanco River basin that was severely affected by the eruption of the Chaitén volcano, begun in May 2008. The eruption triggered secondary events that occurred until February 2009, deeply modifying the forest cover, hydrology and morphology of the area. Further specifics on the eruption and its consequences can be found in Alfano et al. (2011), Major et al. (2013), and Swanson et al. (2013).

3. Methods

3.1. Landslide inventory

Satellite imagery was used to identify landslides in the Blanco River basin. Landslide images were obtained from the Planet Explorer dataset (Planet Team, 2017), and the characteristic of the satellite images used are in Table 1.

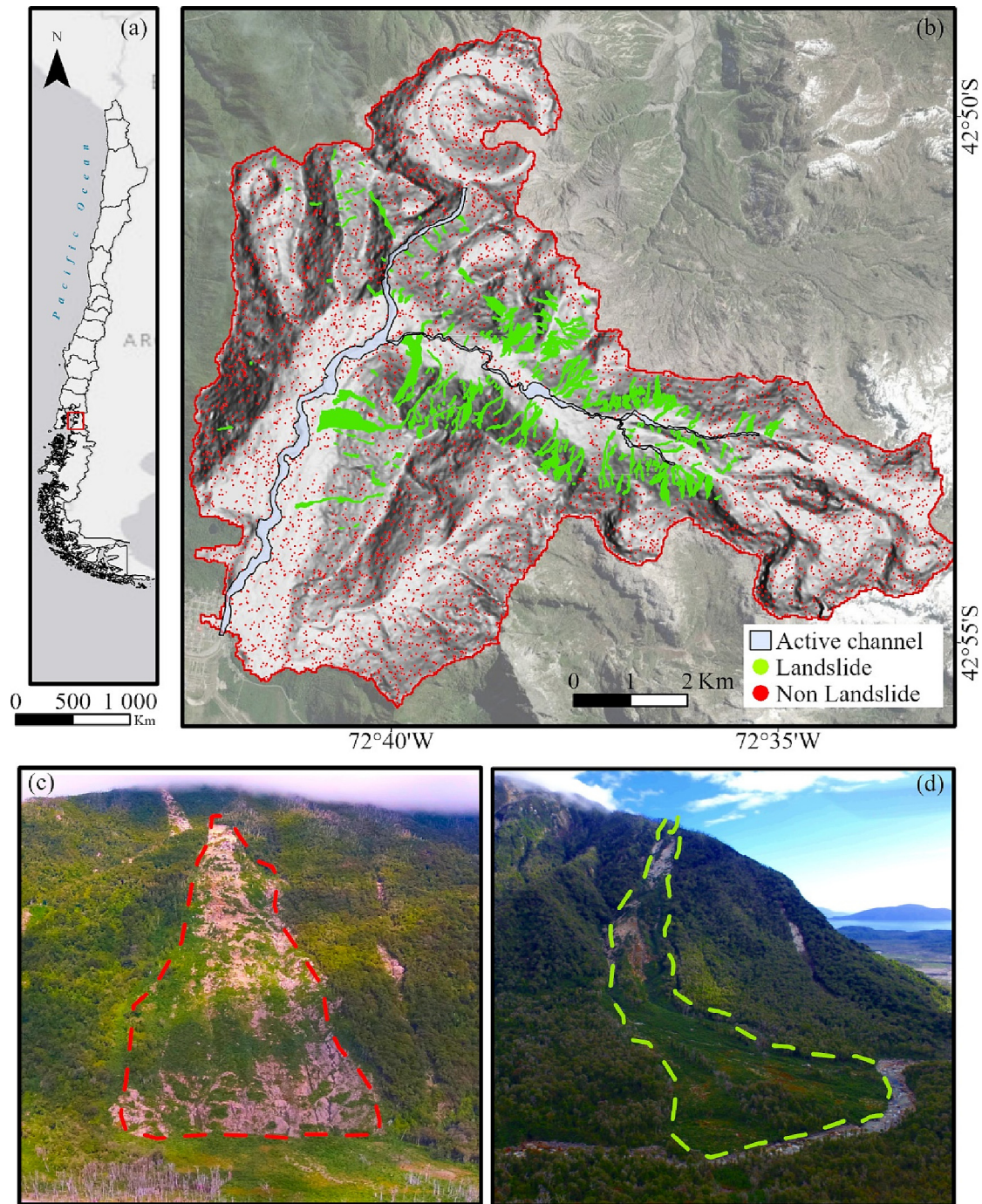


Fig. 1. (a) General location of the Chaitén area. (b) Blanco River catchment, landslide and non-landslide samples (green and red dot, respectively). Images in (b) from Esri service layer and Aster GDEM 2011. Example of (c) disconnected landslide (red), because is not in contact with the active channel, and (d) connected landslide (green), because is in contact with the active channel.

All landslides were mapped in ArcGIS by hand as polygons using visual interpretation and differences in the NDVI series. This means that first, the landslide scars were identified as visible abrupt changes in NDVI values between one year and another, and then the polygons were delimited using ArcGIS Pro 3.0. The high cloud cover during winter means that the images were mainly selected during the summer months when landslide detection is easier.

The polygons include the complete detection area, with the initiation and deposition area. However, we chose to map only landslides larger than four pixels to avoid potential detection errors. Given the minimum resolution of the images (5 m), a lower limit of 100 m² was set for the detection. The mapped landslides were classified as new events or as an

extension of old landslides. For clarification, type I) is a new landslide that appears isolated on the slope without contact with other landslides, and type II is the expansion of an existing landslide.

3.2. Conditioning factors

We used a set of 11 conditioning factors (Table 2) for the construction of the multi-temporal LSM, following the proposals by Morales et al. (2021) and the most relevant factors in the literature.

Topographic factors are extracted from the Digital Elevation Model (DEM) of the study area. We used a DEM with a spatial resolution of 12.5 × 12.5 m, acquired from the open-source website Alaskan Satellite

Table 1

Date, spatial resolution, and sensor of satellite imagery.

Date of acquisition	Spatial resolution (m/pixel)	Sensor
14/12/2010	5	Rapid Eye 2
16/11/2011	5	Rapid Eye 1
17/01/2013	5	Rapid Eye 5
12/01/2014	5	Rapid Eye 3
04/03/2015	5	Rapid Eye 5
10/02/2016	5	Rapid Eye 5
26/01/2017	3.125	PlanetScope
08/01/2018	3.125	PlanetScope
26/01/2019	5	Rapid Eye 3
31/12/2019	5	Rapid Eye 3

Facility (<https://asf.alaska.edu/>). These factors such as elevation, slope, curvature, aspect, and TPI have been used in multiple previous studies on landslide susceptibility due to their high correlation with landslide occurrence (Chen and Chen, 2021; Roy et al., 2022; Spiekermann et al., 2022b). Elevation represents the altitude of land over sea level and controls the temperature, vegetation, and strength of rockfalls (Guzzetti et al., 2012). The angle of the slope is the maximum change in elevation over the distance between pixels and is one of the main factors controlling landslide occurrence (Trigila et al., 2015). Aspect is the direction of the slope to the sun, controlling the weathering rate, moisture content, the impact of rainfall, and abrasion winds (Parra et al., 2021). Curvature is the spatial variation of the degree of slope, which varies between positive (convex), negative (concave), or 0 values (plane) (Minár et al., 2020). TPI represents a measure of the hillslope-scale position, with higher values indicating higher positions (e.g. ridges) (Maxwell and Shobe, 2022). In addition, we included the proximity to the channel network, which generates great influence on the landslide process, saturating the foot of the slopes with water and increasing erosion, thus generating slope instability. We calculated two types of distance to the channel network: I) the vertical distance to the channel network was generated by ArcGIS pro 3.0 flow distance tool-box, II) the horizontal distance to the channel network was prepared in ArcGIS pro 3.0 by using the Euclidean distances (Rabby and Li, 2020; Gaidzik and Ramírez-Herrera, 2021). We extracted five lithological units from the Sernageomin geological map (<https://www.sernageomin.cl/>). Bedrock geology has been shown to control the occurrence of landslides in other areas (Guzzetti et al., 2006). Finally, environmental conditions (NDVI) and pyroclastic deposits (Alfano et al., 2011) were generated from satellite imagery.

We considered the mapped landslides as the dependent variable and 11 conditioning factors (see Table 2 or Fig. S1, supplementary material) as predictor variables for the susceptibility model. Once the landslides were

Table 2

Data sources and conditioning factors.

Type	Spatial Resolution (m)	Conditioning factors	Source
Topographic	12.5	Elevation	Aster Gdem-JAXA (ASF DAAC 2017; Includes Material © JAXA/METI 2011. doi: https://doi.org/10.5067/z97hfcnr6v)
		Slope	
		Aspect	
		Plan curvature	
		Profile curvature	
		Vertical distance to drainage (VDD)	
		Horizontal distance to drainage (HDD)	
Geology	12.5	Topographic Position Index (TPI)	Sernageomin, Chile (Geological map, 2003; 1:1,000,000)
		Lithology	
Environmental conditions	5	NDVI series	Planet Explorer (Planet Team, 2017)
	12.5	Tephra depth	Alfano et al., 2011

delineated as a polygonal layer, we converted them into a landslide occurrence/non-occurrence raster layer. We used the pixel-based or mass point (one point per pixel) sampling techniques to construct occurrence/non-occurrence data (Lima et al., 2022; Pourghasemi et al., 2020; Regmi et al., 2014). The occurrence data was obtained from the pixels within the landslide area, whereas non-occurrence pixels were picked randomly within the basin, but at least 75 m away from the occurrence area to avoid spatial correlation (Lucchese et al., 2021), and in the same proportion as the landslide pixels. The occurrence/non-occurrence data and the 11 conditioning factors were reprojected and resampled with the same resolution and projection as the DEM. The model chosen for prediction was Random Forest (Breiman, 2001) with hyper parametrization in 100 trees (Fig. S2, supplementary material). Studies have shown that Random Forest offers better predictive capacity compared to other susceptibility models (Emberson et al., 2021a; Lombardo et al., 2020; Reichenbach et al., 2018; Tanyu et al., 2021).

3.2.1. Multi-collinearity diagnosis and selection of conditioning factors

Before constructing the LSMs, the multicollinearity of the conditioning factors was assessed. To detect high correlations between factors, three statistical tests were used; the variable inflation factors (VIF); the tolerance (TOL); and the Information Gain Ratio (IG). These tests have been widely used in previous research (Lombardo et al., 2020), with TOL <0.1 or VIF >10 indicating the existence of multicollinearity. IG is an entropy-based feature evaluation method. It is defined as the amount of information provided by the conditional factors for the landslide susceptibility analysis (Tanyu et al., 2021). The mean of these three indicators for the entire training dataset was calculated and presented as supplementary material (Table S1, supplementary material). Moreover, the role of the conditioning factors with the highest IG was further investigated using their regression coefficients extrapolated during the model building (Section 3.3).

3.3. Landslide susceptibility model

The implementation of LSM was accomplished with three phases: calibration, testing phase, and prediction. Calibration and testing phases were conducted using an 80/20 proportion (each year 80 samples for calibration and 20 for testing) and only type I landslide to avoid spatial correlation in the testing phase. During the calibration phase, the Random Forest was computed through the three times 10-fold cross-validation method and, the optimal cutoff along the ROC curve (i.e., the best probability distinction between occurrence and non-occurrence) was determined on the basis of Youden's J.

To validate the prediction power of each year model, the third phase was carried out using type I and type II landslide of the next year, as a new independent dataset. In this way, all data from the following years are used to evaluate the temporal variation in LSM (e.g., 2010 model used to predict 2011 data). For the performance evaluation the following metrics were used: the area under ROC curve (AUC), accuracy, specificity, sensitivity, kappa coefficient, and the confusion matrix (CM). The ROC is a probability curve obtained by plotting the true positive rate (TPR) against the false positive rate (FPR). TPR is the proportion of the presence of landslides correctly classified as landslides. FPR is often referred to as 1-specificity and is the percentage of landslide absences that were incorrectly classified as landslide presences. The Kappa coefficient was used to verify the consistency between the prediction model results and the actual situation. The CM was calculated to analyse the prediction accuracy of the model, the main contents of the confusion matrix are TP, TN, FP and FN representing results partitioned into four cases (Morales et al., 2021). Accuracy, specificity, and sensitivity represent model prediction performance (Emberson et al., 2021). This parameter are defined as follows:

$$\text{Accuracy} = \frac{\text{TP} + \text{TN}}{\text{TP} + \text{TN} + \text{FN} + \text{FP}} \quad (1)$$

$$\text{Specificity} = \frac{\text{TN}}{\text{TN} + \text{FN}} \quad (2)$$

$$\text{Sensitivity} = \frac{\text{TP}}{\text{TP} + \text{FN}} \quad (3)$$

where TP (true positive), is a landslide occurrence that is correctly classified; FP (false positive) landslide occurrence that is misclassified; TN (true negative) non-occurrence that is correctly classified; and FN (false negative) non-occurrence that is misclassified.

Since many conditioning factors have different evolution after being affected by a volcanic eruption, it is necessary to study the importance and stability of the conditioning factors over time to provide guidelines for predicting and preventing landslide disasters. The importance and stability of the 11 final conditioning factors were analyzed using the regression coefficients extrapolated from each random forest model. All analyses were carried out using the Caret 6.0v (Kuhn, 2008) and CAST 0.7v (Meyer et al., 2023) packages in statistical software R and Rstudio (see <https://www.r-project.org/>).

3.4. Lateral connectivity mapping

The proxy for sediment routing in this work was represented by the IC (Cavalli et al., 2013), which was implemented for its capacity to depict coupling relationships with landslides-channel (i.e. lateral connectivity). Therefore, the IC was used to derive a unique thresholded connectivity map for 2019, where high and low connectivity are objectively identified through logistic regression analysis. First, the IC was computed for the Blanco River catchment primarily following the methodology proposed by Martini et al. (2019). Summarizing: i) the input DEM was the same as for the LSMs (12.5 m resolution); ii) an adaptive W factor was generated using field surveys and image classification technique to spatialize ad-hoc Manning's coefficients; iii) the 2019 Blanco River active channel was outlined as the target of the IC by considering the zones of visible river influence.

The IC computation was accomplished via standard R_IC (Martini et al., 2022b), an open-source tool in an R environment, and available in Baggio et al. (2022). Once the 2019 IC map was obtained, the connectivity status of the landslides was established, considering two possible situations: disconnected, when the landslide is not in contact at all with the target (Fig. 1c); or connected, when the landslide is in contact with the target, i.e. active channel (Fig. 1d). The assessment was performed by visual inspection of the 2019 satellite image (Table 1). For the purpose of the connectivity analysis, we considered all cumulative landslides visible in 2019, hence the sources were not discriminated in type I or II. As result, 186 landslides were used for the development of the next step: the logistic regression analysis following the methodology published in Martini et al. (2022a). First, a logistic regression model was trained using the connectivity status (connected vs disconnected) as response variable and the median IC value extrapolated for each landslide as predictor. The IC values extrapolated for the two groups (connected and disconnected) were tested for difference using the Mann-Whitney test ($\alpha = 0.05$).

Second, repeated k-folds cross-validation was implemented to handle potential imbalance datasets and to feed a logistic regression model (binomial GLM). The performance was evaluated using the accuracy and the AUC values, which pose specificity against sensitivity (Bradley, 1997). Finally, the optimal cutoff (i.e. the best probability discriminator between connected and disconnected) along the ROC curve was identified based on Youden's J. With the optimal cutoff it was possible to derive a crisp IC threshold, discriminating the IC map between connected and disconnected areas.

4. Results

4.1. Landslide inventories and condition factors assessment

We identified a total of 415 landslides between 2010 and 2019, 294 types I and 121 types II. After 2010 an increase in the frequency of landslides

is observed, peaking at 97 events in 2012 alone. After 2014, the number decreased constantly year by year, reaching 16 in 2019. However, a greater increase in the overall area affected is observed in 2015, in which 130.726 ha were activated. The lowest increase is 9.41 ha in 2018. The total area affected by landslides reached 390 ha at the end of the study period (Fig. 2).

Concerning the variable assessment importance, the regression coefficients of the four most important factors according to the highest IG (Section 3.2.1) are presented in Fig. 3. These outputs underline the multi-temporal influence of tephra, NDVI, elevation, and slope on the LSMs. The regression coefficients for NDVI were more variable than tephra (Fig. 3a). The first three years were consistently highly negative, hence lower the NDVI and higher landslide occurrence, followed by three years (2013–2015) of positive coefficients but around zero and, after that, large fluctuations with even high positive values in 2018. Therefore, even if NDVI was found highly impactful, its relationship with landslide occurrence was not always inversely proportional. In Fig. 3b and Fig. 3c it is possible to observe the results for topographic factors, elevation and slope, respectively. Both were stable during the study period, in the sense that they were always all negative or positive, suggesting that the former was decreasing the probability of land sliding and the latter increasing it. Finally, the tephra depth (Fig. 3d) shows always positive median values, indicating that, overall, the deeper the tephra layer the higher the landslide occurrence. However, in some years the coefficient distribution of tephra depth indicates the presence of inverse relationship in some models (negative 1st quartiles).

4.2. Landslide susceptibility model performance

4.2.1. Calibration phase

The model calibration phase produced ten LSMs and the metrics used to evaluate the performance of the model are shown in Table 3. The performance metrics show slight variation between the models, with the highest accuracy and kappa value in 2017 (0.987 and 0.975, respectively) and the lowest value in 2018 (0.943 and 0.886, respectively). For the whole study period, the mean accuracy is 0.97 and the mean value of the kappa index is 0.94. Thresholds are also reported to highlight the variability in the cutoff during the period.

Fig. S3 (supplementary material) shows the AUC values for the calibration phase. This quantifies how accurately the models trained on 1 year using k-fold cross-validation. The boxplot shows the variation in AUC produced by all the possible combinations generated by the k-folds cross-validation. The maximum variation is observed in 2018, with the minimum going lower than 0.9. The great variability shown in this year can be ascribed to the lowest of events observed (Fig. 2).

4.2.2. Testing phase

Table 4 describes the outcomes of confusion matrixes of the testing phase. In general, the high values of TNR and TPR in the ten confusion matrixes reflect the good performance of the models already presented in

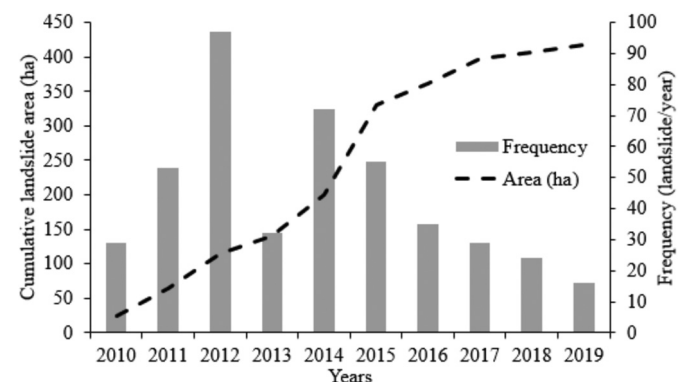


Fig. 2. Landslide frequency (bar plot) and cumulative area affected by landslide (dashed black lines).

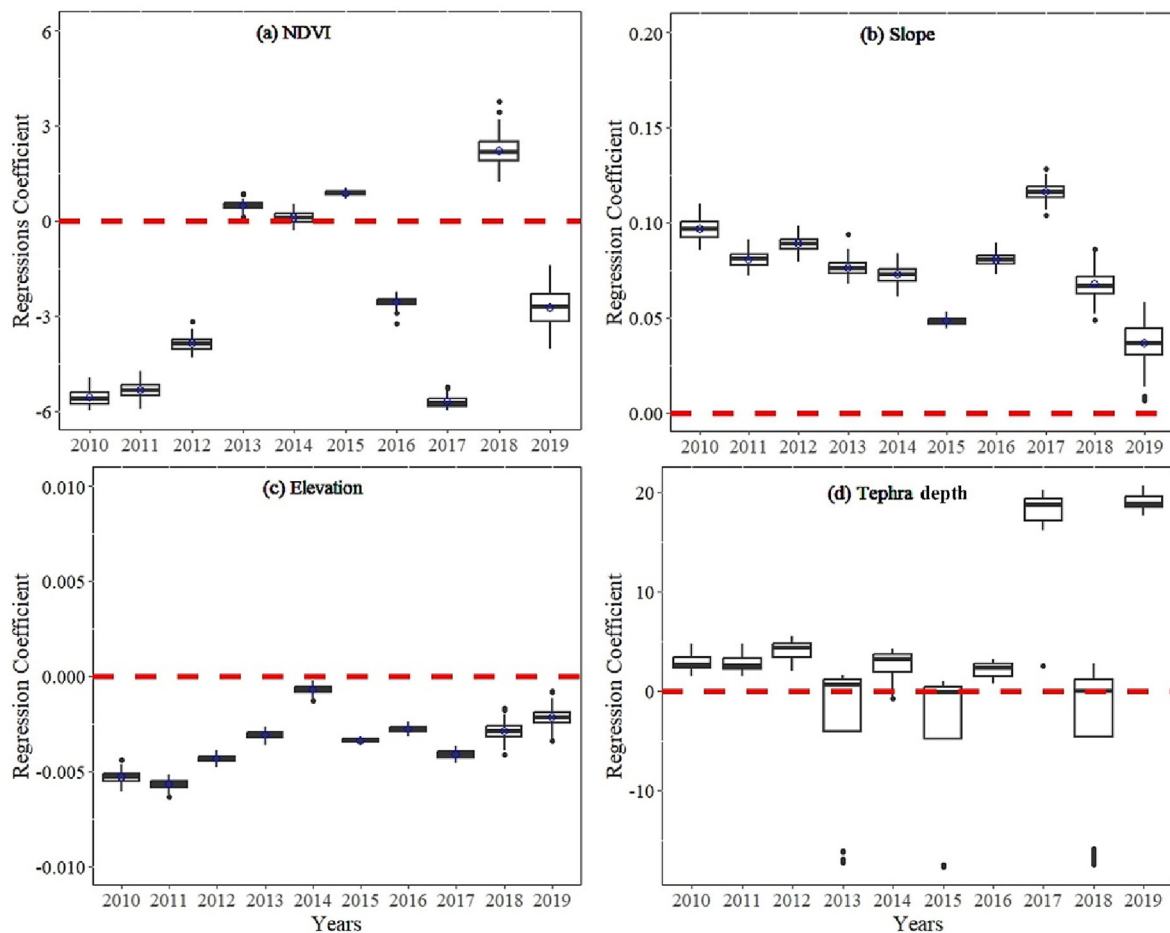


Fig. 3. Boxplots represent the regression coefficients calculated from 100 bootstraps models run per year. The red line shows the 0-line of the regression coefficient axis. In box plots, the lower box boundary indicates the 25th percentile, a black line inside the box indicates the median, and the upper box boundary indicates the 75th percentile. Black dots above and below the whiskers indicate outliers outside the 10th and 90th percentiles.

Table 3. In the confusion matrixes, the 2010 model had the highest TPR of 52.2 % and the lowest TPR can be found in 2011 at 31 %; while the 2011 model had the highest TNR of 67 % and the lowest TNR can be found in 2010 at 43 %. The models with highest FPRs are in 2018 (6.8 %) and in 2019 (3.6 %). Overall FPR values vary between 1.2 % and 6.8 %, hence still maintaining low values of misclassification among the models. Overall FNR values are lower than 1.5 %, therefore, indicating only few landslides detected as non-occurrence.

Fig. S4 (supplementary material) also reports the ROC curves of the models for the testing phase. The AUC values change slightly, the variation is relatively concentrated, and these results show that the models are stable. Overall, all the AUC values are extremely high (>99 %),

confirming the good performance already reported in the calibration phase (4.2.1).

4.2.3. Prediction phase

The confusion matrix computed for the prediction phase is shown in **Table 5**. The highest TPR of 40 % is in 2010, the 2011 and 2012 models had the highest TNR of 60.6 %. The FPR with high values is the 2016 model with 6.6 %. Concerning FNR, is possible to observe low values in the first three years, followed by a rapid increase in 2013 where FNR grew up to 36 % (2017). Still after 2017, the FNR shows high values,

Table 4

Results of the confusion matrix for each year's model based on the relation between observed data and predicted data for the testing phase; in parentheses the number of pixels (n. of samples). Four metrics are reported (see **Section 3.3**): True Positive Rate (TPR), False Positive Rate (FPR), False Negative Rate (FNR) and True Negative Rate (TNR).

Table 3
Accuracy, Kappa, and threshold for RF models.

Year	Accuracy	Kappa	Threshold
2010	0.944	0.886	0.4
2011	0.978	0.950	0.55
2012	0.975	0.949	0.5
2013	0.961	0.921	0.4
2014	0.980	0.959	0.4
2015	0.969	0.939	0.45
2016	0.967	0.933	0.5
2017	0.987	0.975	0.45
2018	0.943	0.886	0.45
2019	0.978	0.957	0.5
Mean	0.97	0.94	0.46

Year	TPR % (n)	FPR % (n)	FNR % (n)	TNR % (n)
2010	52.2 (210)	3.2 (13)	1.5 (6)	43 (173)
2011	31 (211)	1.2 (8)	0.9 (6)	67 (456)
2012	49.4 (585)	1.8 (21)	0.7 (8)	48.1 (570)
2013	49.4 (379)	3.3 (25)	0.8 (6)	46.5 (2)
2014	49.7 (284)	3.2 (18)	0.4 (2)	46.8 (267)
2015	49.7 (1389)	2.1 (60)	0.4 (2)	47.7 (267)
2016	48.9 (486)	1.3 (21)	1.2 (12)	48.6 (483)
2017	49.7 (502)	1.2 (12)	0.5 (5)	48.6 (491)
2018	49.3 (72)	6.8 (10)	0.7 (1)	43.2 (63)
2019	48.9 (68)	3.6 (5)	1.4 (2)	46 (64)

Table 5

Results of the confusion matrix for each year's model based on the relation between observed data and predicted data for the prediction phase; in parentheses the number of pixels (n. of samples). Four metrics are reported (see Section 3.3): True Positive Rate (TPR), False Positive Rate (FPR), False Negative Rate (FNR) and True Negative Rate (TNR).

Year	TPR % (n)	FPR % (n)	FNR % (n)	TNR % (n)
2011	40 (2162)	2.3 (124)	0.1(6)	57.6 (3114)
2012	31.3 (933)	0.5 (15)	7.6 (228)	60.6 (1808)
2013	31.3 (935)	0.5 (15)	7.6 (227)	60.6 (1810)
2014	16 (679)	1.4 (59)	20 (850)	62.6 (2663)
2015	6 (447)	0.8 (57)	33.2 (2475)	60.1 (4486)
2016	20.5 (1809)	1 (86)	20.2 (1781)	58.3 (5131)
2017	6.1 (623)	6.6 (669)	36 (3661)	51.2 (5205)
2018	19.8 (2044)	0.5 (54)	22.2 (2285)	57.5 (5924)
2019	9.1 (952)	1.7 (176)	33 (3451)	56.3 (5892)

indicating a reduced capacity of the model to predict landslide occurrence. For the final map of 2019, the results show a TPR, TNR, FPR and FNR of 9.1 %, 56.3 %, 1.7 %, and 33 %, respectively.

Fig. 4 shows the spatial distribution of the susceptibility through prediction maps generated by random forest models for each year. The results showed that the probability of landslides is mainly restricted to areas highly affected by tephra falls. As altitude increases in the catchment, the probability of landslides begins to be distributed mainly in steep and confined slope morphologies. The north part of the study area stood out with a high probability of landslides, concentrated mainly on high-altitude hillslopes. However, considering the temporal range analyses, the western part of the Blanco River basin did not present greater susceptibility in the first 6 years, after which an increase in the probability of landslides is observed. On the contrary, high susceptibility areas were mainly restricted to the NE of the catchment. These areas are valleys discharging waters from the Michinmahuida glaciers, characterized by steep slopes and confined channels until the confluence with the Caldera Creek.

4.3. Connectivity mapping

Potential sediment transfer pathways can be observed in the IC map (Fig. 5a), which quantifies the degree of linkage between hillslopes and

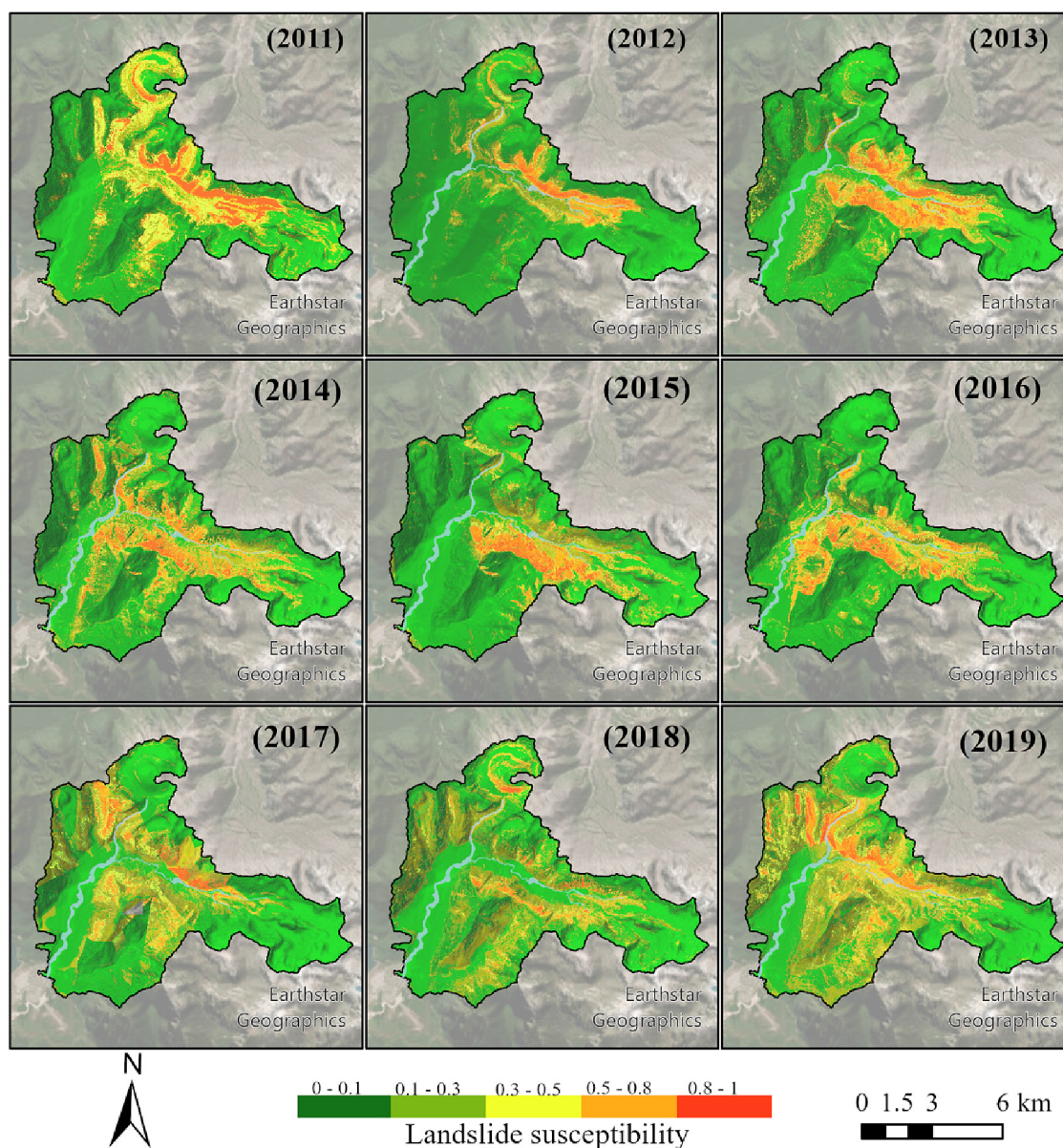


Fig. 4. Landslide susceptibility maps predicted using the antecedent year's model (1 indicates high susceptibility and 0 low susceptibility).

active channel. The IC is higher in specific areas of the catchment: along the Caldera Creek and in the upstream part of the main Blanco River, where the valley features a W-SE orientation. Particularly, in these areas, the degree of connectivity is boosted by the presence of steep and confined slopes, potentially supplying sediment without any significant landform impediment. On the contrary, the IC is lower where the active channel is far from the hillslopes (e.g. caldera and the SE subbasin) or where the valley bottom is wide and prevents a direct coupling hillslopes-channel. This is the case of the main Blanco River channel that flows unconfined almost everywhere from the confluence with the Caldera Creek to the outlet. Here the flood-plain acting as a buffer prevents sediment contribution from the hillslopes.

The assessment of connectivity status conducted using the aerial images led to the identification of 132 landslides disconnected and 54 connected to

the active channel (Fig. 5b). The former are covering a total surface of 178 ha (2.5 % of the catchment) with a mean area of 3.3 ha, while the latter are covering 213 ha (3 % of the catchment) with a mean area of 1.6 ha. Looking at the spatial arrangement, it is possible to observe that there are no connected landslides in the main and wide Rio Blanco valley (N-S orientation). On the contrary, all the connected areas are located where the active channel is narrower and the valleys more confined. Furthermore, it is possible to spot a group of disconnected areas in small sub-basins, east to the Caldera Creek, where the long distance and the topographic position (overhanging plateau) are preventing the sediment coupling with the active channel.

Concerning the IC values extrapolated for each area, the minimum, median, and maximum values are -2.7 , -0.11 , 0.62 , and -3.6 , -2.1 , 0.28

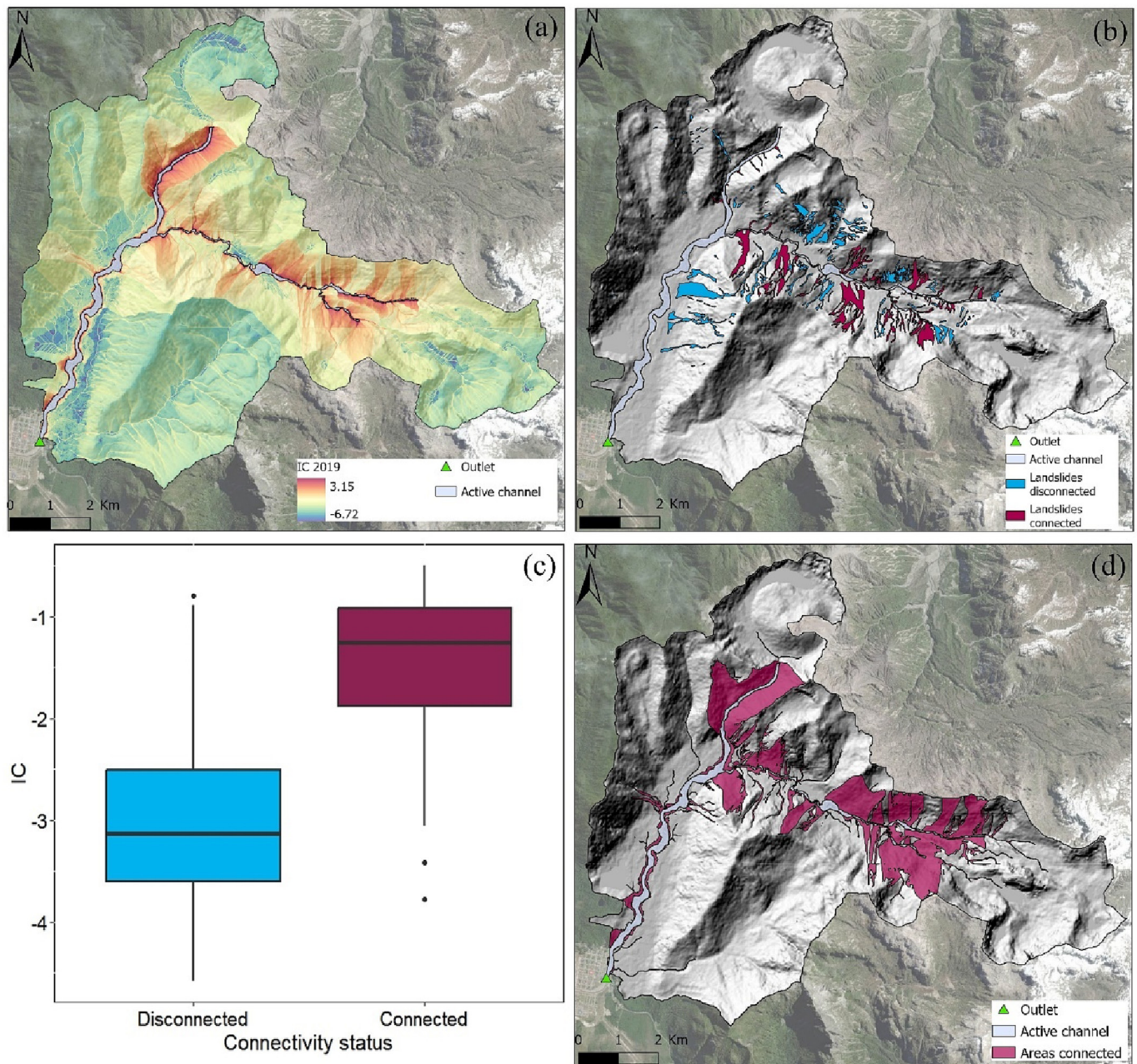


Fig. 5. Sediment connectivity mapping for the 2019 year. (a) Index of Connectivity map, showing high (red) to low (blue) IC values with reference to the active channel. (b) The cumulated landslide inventory classified according to the connectivity status. (c) Boxplots showing the distribution of IC values extracted for each of the disconnected and connected landslides. The lower box boundary indicates the 25th percentile, a black line inside the box indicates the median and the upper box boundary indicates the 75th percentile. Black dots above and below the whiskers (1.5 times the interquartile range) indicate outliers. (d) High sediment connectivity in the Blanco River catchment is highlighted in areas where the IC threshold (-1.37) is exceeded.

for connected and disconnected, respectively. This difference can be even more appreciated from Fig. 5c, where the distributions are reported in the form of boxplot charts. Disconnected landslides are visibly showing lower values than connected ones, in this way favoring the predictive capacity of the logistic regression model. This difference is supported by the Mann-Whitney test results, which reports statistical difference between the two groups (p -value < 0.05). The logistic regression model found statistical significance between IC and connectivity status (p -value < 0.001). Moreover, the model performed well to discriminate disconnected and connected landslides; the accuracy, sensitivity, and specificity are 0.82, 0.69, and 0.87, respectively. Consequently, the AUROC is 0.897 (Fig. S5, supplementary material). Analyzing the Youden's J, which describes the performance of different probability cutoffs, the results showed an optimum cutoff equal to 0.18, which corresponds to an IC value of -1.37 . This value was then used as a threshold to classify the 2019 IC map characterized into connected (> -1.37) and disconnected (< -1.37) areas (Fig. 5d).

4.4. Connectivity index and landslide susceptibility

The combination of the landslide susceptibility map and connectivity map for the year 2019 is presented in Fig. 6. As visible, most of the basin (79.9 %) displays areas not susceptible to landslides and disconnected

from the Blanco River active channel. This comprehends for instance the areas of the headwaters, characterized by snow cover and large distance to the target. Orange areas indicate areas susceptible but disconnected (5.9 %), hence prone to sediment source activation but not capable of delivering the sediment into the Blanco River system. A good example is represented by a large zone west of the Caldera Creek, where the steep slopes are susceptible to landslide occurrence but disconnected by the presence of the wide floodplain. On the other hand, areas connected but not susceptible (10.9 %) are represented by those slopes in which the concept of sediment connectivity remains only potential, i.e. a hypothetical sediment transfer from source to channel. Finally, 3.1 % of the basin is characterized as areas susceptible and connected. These are mainly clustered in three zones, along the Caldera Creek, on the right slopes just upstream of the confluence and more upstream where the active channel is wider and closer to the steep slopes.

5. Discussion

5.1. Landslide inventory, conditioning factors performance and evolution

Concerning the frequency and temporal evolution of the areas covered by landslides, our results are partially in agreement with the report by Korup et al. (2019), which observed an increase in the number of landslides

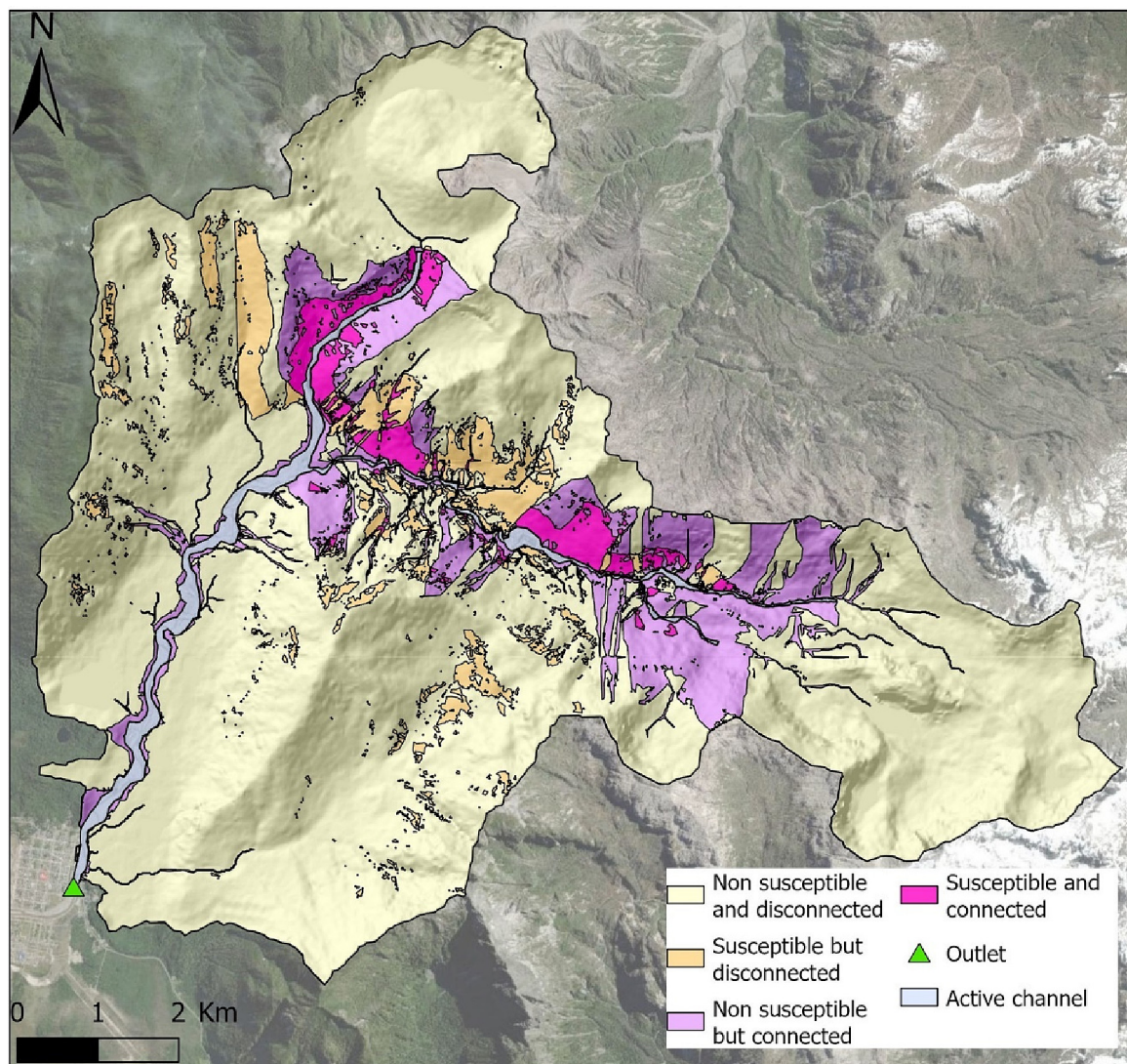


Fig. 6. The joint 2019 landslide susceptibility-sediment connectivity map. Four classes are derived from the combination: non susceptible and disconnected; susceptible but disconnected; non susceptible but connected; susceptible and connected.

starting in 2012 (4 years after the initial phase of the eruption). In the Blanco River catchment, we observed an increase in number of events already from 2010. Nonetheless, the maximum peak in numbers and area affected was between 2012 and 2016, reporting 259 landslides and an affected area of 335 ha, respectively (Fig. 2). However, we observed a decrease in the occurrence and size of landslides in the years following 2017.

Similar to other studies worldwide (Lombardo and Mai, 2018; Emberson et al., 2021; Sun et al., 2020; Lima et al., 2022), topographic conditions (aspect, slope, and elevation) in our models were found highly important predictors (0.07, 0.06 and 0.08 IG, respectively). In contrast, the curvature conditions (planform and profile) showed low importance values in all models (0.01 and 0.01 IG, respectively). The reason for this may be due to the DEM resolution (12.5×12.5 m), which generates smoothing of the terrain, decreasing the importance of these conditioning factors as predictors (Lima et al., 2022). Recent studies show that the use of higher resolutions would improve the topographic effects along and across the slopes, allowing a more advanced understanding of susceptibility from a geomorphological point of view (Gaidzik and Ramírez-Herrera, 2021; Lizama et al., 2022). The VDD showed average IG values (0.04), these initial depression points accumulate the flow of water from nearby hillslopes, becoming important hydrological triggers for landslides (Parra et al., 2021). We found that environmental factors (NDVI and tephra) were the most important predictors, presenting the highest IG values. This was due to the great impact suffered by the eruption of the Chaitén volcano, which buried a large part of the northeast area of the basin with large volumes of pyroclastic materials (Alfano et al., 2011). Particularly, NDVI values decrease in areas where pyroclastic deposits cover native vegetation, gradually reducing the root resistance of decaying trees and reducing slope stability after tree dead of trees (Korup et al., 2019; Major et al., 2013).

In the north Patagonian context, two studies were conducted regarding landslide detection. First Morales et al. (2021) highlighted the most important factors affecting landslide detection in the last 19 years, among which they reported: time after the eruption of the Chaitén volcano, tephra depth, and distance to the Liquiñe-Ofqui fault. Furthermore, they reported significant values in the topographic predictors used also in our research (slope, elevation, aspect). Second, our outcomes differ from those found by Lizama et al. (2022), who performed a susceptibility modeling in Lake Yelcho catchment, close to the Blanco River catchment, in which the elevation and depth of tephra showed low prediction coefficients. The different characteristics of the studied catchments explain this behavior. While the Blanco River catchment was directly affected by the eruption of the Chaitén volcano, recording in some areas tephra depths >100 cm, the Lake Yelcho catchment records a maximum tephra depth of 1 cm (Alfano et al., 2011).

Focusing on the evolution of the conditioning factors within the study area, overall, regression coefficient analyses (Fig. 3), showed that topographic conditions widely used in susceptibility models, such as slope and elevation (Lima et al., 2022), had a stable trend for the whole nine-year period. These results are like those of Lombardo and Mai (2018), in which slope and elevation are part of the most stable and important factors for landslide models. On the other hand, NDVI and tephra depth showed the highest temporal variations, suggesting changes in the spatial distribution of landslides during the study period. Our results showed that during the first 3 years of analysis (5 years after eruption), the highest density of landslides occurred in areas strongly affected by tephra fall, where the most severe effects on vegetation were recorded, and where low values of NDVI were recorded (mean value of NDVI in zones of occurrence = 0.3). Whereas, from 2013 to 2016 and in 2018, landslides were recorded in zones with lower tephra depth, where only slight disturbed vegetation was observed (mean value of NDVI in zones of occurrence = 0.6). This explains the positive regression coefficients and the great variability underlined in the NDVI and tephra depth (Fig. 3a and d).

Therefore, it is evident a clear temporal variability in the performance of certain conditioning factors (NDVI above all). These results are similar to those of Jones et al. (2021), who found that the performance of the conditioning factor is influenced by different triggers, which results in changes

in the spatial distribution of landslides and affects the predictive capabilities of models trained in years of extreme disturbance.

5.2. Connectivity models

After the Chaitén eruption, the Blanco River catchment underwent a period of high dynamism, especially along the main channel, where evident changes in LW load, vegetation characteristics, and morphology have been reported (Ulloa et al., 2016; Tonon et al., 2018; Iroumé et al., 2020). Furthermore, also the hillslopes responded to the tephra loads by increasing landslide activity and sediment connectivity (Martini et al., 2019). The results are in line with Ortíz-Rodríguez et al. (2020), who reported increased hydrological and sediment connectivity in multiple basins affected by the eruption of the Colima and Popocatepetl volcanoes in Mexico.

Considering the connectivity results of this research and the areas classified as connected by the logistic regression analysis (either red area in Fig. 5d or purple plus pink areas in Fig. 6), this information still can i) be subjected to a certain error and ii) remain only theoretical if no other functional aspects are introduced. On one hand, without the involvement of external triggering factors directly into the IC computation, above all hydro-meteorological data (Heckmann et al., 2018), the outcome is expected to be more a structural illustration of connectivity, hence not entirely capable of predicting event-based sediment dynamics or long-term estimates of sediment yield (Wu et al., 2023). On the other hand, it is important to remind that the IC applied in this research (Cavalli et al., 2013) is designed as a topography-based index, hence it is not expected (and should not be expected) to function as a physical model.

To bypass this issue, in this study we introduced another source of information to map sediment connectivity from sources to channel more usefully. The combination with landslide susceptibility map shifted the representation of sediment transfers from theoretical to more practical. The joint susceptibility-connectivity map allowed to further prioritize the catchment by pointing out true hot spots (susceptible and connected) from only potential hot spots (non-susceptible but connected; susceptible but disconnected).

The generation of thresholding-connectivity maps and their validation, i.e. discriminating between true connected and disconnected areas according to a robust statistical methodology, is surely one of the novelties and challenging aspects of the recent investigations in the field of sediment connectivity (Hooke and Souza, 2021). The methodology proposed in this work is similar to the one proposed by Martini et al. (2022a) and Steger et al. (2022) in the Alps. However, the very different environmental characteristics and data quality of the Chaitén area affected the transferability of their approach and indeed the overall result. The presence of a dense forest cover, the effects of the eruption, and the low DEM resolution led to inevitable adaptations in all parts of the workflow. As consequence, as already stated, the final connectivity-susceptibility map can be subjected to more uncertainty than those generated in the Alps.

The performance assessment for the connectivity logistic model reported good results but with room for improvement (AUC 0.82). The consequences might be misclassification errors in future (post-2019) predictions. An example is already offered by a new landslide appeared after 2019 in an area classified as connected (> -1.37) but evidently disconnected from the active channel probably due to a decoupling condition exerted by a forested flat buffer and large wood accumulation at the bottom of the hillslope (Fig. 7). Predicting hillslope-channel coupling condition of landslides is largely dependent on specific factors such scar size, area and run-out distance. However, their involvement in a landslide connectivity model can be a trade-off between higher performance and the difficulty of retrieving such data (Spiekermann et al., 2022b).

5.3. Uncertainties of the LSMs

The methodology implemented in the present study allowed us to develop a susceptibility model for the period 2010–2019 using a set of conditioning factors which considered the topography, geology, and

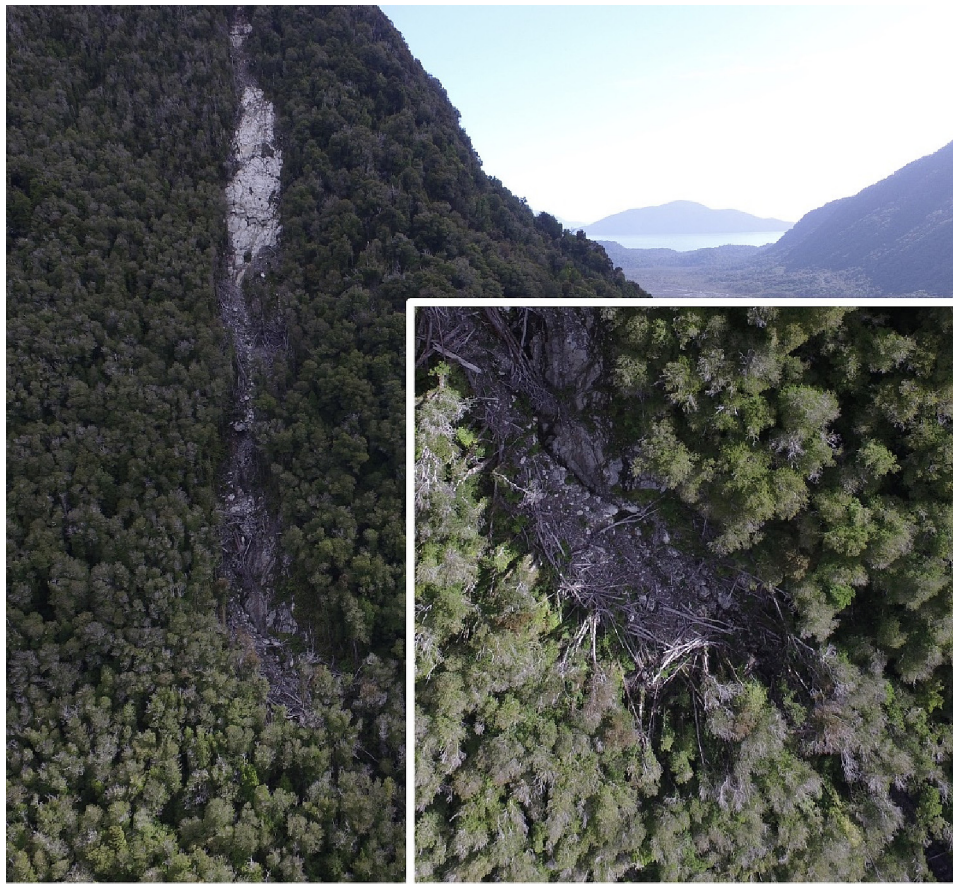


Fig. 7. Photos of a new landslide that occurred after 2019 in the Blanco River catchment. The sediment source is disconnected to the active channel due to the presence of a dense and flat evergreen forest and large wood accumulations.

environmental conditions. Our results show that: (a) there is variation in the performance of landslide conditioning factors over time; (b) there is spatial variation in landslide susceptibility results over time; and (c) results improve when models are developed using stable conditions but are not able to predict highly dynamic environmental changes. In the case of the landslide susceptibility problem, which was expected to avoid erroneous detection of areas where landslides were likely to occur, the model presented high classification values in the calibration phase, which was evaluated through cross-validation (Table 3 and Fig. S3). The testing phase showed high predictive capability, highlighting the good performance of the model in stable environments. However, the prediction phase showed great variability in predictive capacity (Table 5). The most concerning issue is the increase in FNR values and the decrease in TPR from 2013. The increase in FNR values from 2013 indicates a reduction in the predictive capacity of landslide susceptibility. This strong reduction is associated with the occurrence of landslides in areas showing high NDVI values, as also previously mentioned. However, high NDVI values are biased by the rapid colonization of fast herbaceous species, hence favoring the prediction of FN (Knoflach et al., 2021; Saito et al., 2022). The role of vegetation is fundamental to controlling slope stability (Murgia et al., 2022). The existence of trees has been shown to reduce erosion caused by surface landslides by 16.6 % to 42.9 % (Spiekermann et al., 2022b). Nevertheless, appropriate heights and densities are needed, e.g. tall but scattered trees are not able to prevent a landslide. (Tsunetaka et al., 2022; Micheline et al., 2017). Fig. 8 shows an example of rapid re-vegetated landslides, which contribute to increase FNR values. In this case, the endemic *Gunnera tinctoria*, has quickly colonized unstable volcanic soils (Skeffington and Hall, 2011) but it does not contribute to the stabilization of the landslide's scar. In this framework, studies show that in order to achieve the recovery of vegetation to its pre-eruption state, longer time periods are necessary

(Biass et al., 2021; Easdale and Bruzzone, 2018; Major et al., 2018; Teltscher and Fassnacht, 2018).

5.4. Insights for catchment management

In mountain catchments, the detection of connected areas represents a fundamental information for optimizing management interventions and further improve risk assessments. Connected sediment sources are those areas more prone to deliver sediment into the channel network, potentially providing an additional sediment input during events. Compared to past applications of the IC, the joint susceptibility-connectivity approach offers a much more robust and reliable tool for predicting sediment transfers from hillslopes to channels during large disturbances. This will improve the capacity of catchment's management strategies to identify how and where to suppress or enhance one or more linkages, switching on and off specific (dis)connectors (Poeppl et al., 2020). Specific practices can include i) selection of active slopes or single sediment sources to be stabilized, ii) planning the arrangement of channel control structures (e.g. check dams) along the channel network, iii) construction of hydraulic structures (e.g. bridge, hydropower facilities) in specific spot with lower level of risk. Furthermore, the susceptibility-connectivity approach can be implemented according to different scenarios. Rather than the active channel, the joint map can be computed with reference to any specific target within the catchment worth to be considered (e.g. outlet, sensitive infrastructures, specific sections of the channels). Scenario-based solutions are clearly dependent on the objective of the study, which in turn must be related to the management goal intended to be achieved. Only in this way, different maps could communicate tailored information following the needs of different stakeholders. Especially in river basins affected by volcanic eruptions, the mitigation of cascading effects induced by this type of disturbance is vital

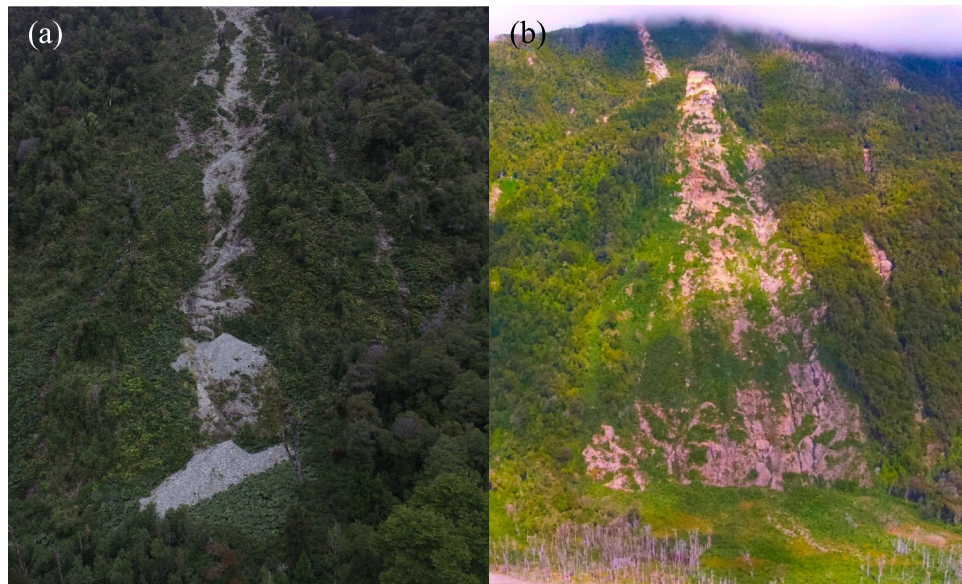


Fig. 8. Examples of landslides colonized by sparse vegetation that do not have a stabilizing effect. (a) a landslide scar still in activity although the presence of vegetation; (b) landslide recolonized with *Gunnera tinctoria*.

(Major et al., 2016). In the Chaitén area, where the assessment of flood hazards caused by river adjustments is still of utmost importance (Basso-Báez et al., 2020), a multi-scenario analysis of landslide susceptibility-connectivity could be the missing link between hillslope processes and downstream river dynamics.

6. Conclusions

In this work, we analyzed the Blanco River catchment, affected by the Chaitén volcanic eruption in 2008–2009, using a combined approach based on landslide susceptibility models and a threshold-based sediment connectivity map. For modeling landslide occurrence, our results indicated that the depth of tephra significantly impacts susceptibility, followed by elevation, NDVI, and slope. Furthermore, we observed that the environmental disturbance generated variations in conditioning factors, decreasing the predictive capacity of the models in highly changing environments such as a catchment recently affected by volcanic eruption. Based on our results, we believe that this spatial-temporal variation of conditioning factors, caused by different levels of disturbance, increase the uncertainty of the susceptibility models (Section 5.3), as reported by the constant change of the susceptibility values over time. Nevertheless, the compound use of landslide susceptibility map and threshold-based connectivity map gave plausible outcomes and important insights on how to move toward a more quantitative analysis of sediment transfer in disturbance-affected catchments. A mutual benefit is indeed evident with this novel approach. On one hand, susceptibility maps can be enriched with information on where to prioritize the landslide occurrence, so that only connected areas are considered. On the other hand, connectivity maps can be greatly improved, shifting from a mere structural and static representation of sediment transfers to a more functional and dynamic one.

Finally, the proposed work establishes a new framework to better understand the hillslope dynamics in a basin widely studied since 2008. In this sense, the same approach could be transferred to other study areas severely affected by large natural disturbances such wildfires, earthquakes, storms, and, of course, volcanic eruptions.

CRediT authorship contribution statement

Alberto Paredes: Methodology, Formal analysis, Investigation, Writing – original draft. **Lorenzo Martini:** Conceptualization, Methodology, Investigation, Writing – original draft. **Andrés Iroumé:**

Conceptualization, Writing – review & editing, Supervision, Project administration. **Lorenzo Picco:** Conceptualization, Writing – review & editing, Supervision, Project administration.

Data availability

Data will be made available on request.

Declaration of competing interest

The authors declare that they have no known competing financial interests or personal relationships that could have appeared to influence the work reported in this paper.

Acknowledgments

This research is supported by a Ph.D. scholarship to the first author granted by Agencia Nacional de Investigación y Desarrollo (ANID) of Chile (Beca Doctorado Nacional No. 21211121). The authors are grateful for the support of the Graduate School of the Faculty of Forest Sciences and Natural Resources, Universidad Austral de Chile, through the use of infrastructure. This research was developed within the frame of the FONDECYT 1200079 funded by the Chilean Government. We acknowledge the support of Planet's Education and Research (E&R) Program. Finally, this research was partially developed within the project financed with BIRD 2021 funds, Dept. TESAF, Università degli Studi di Padova. The authors wish to thank the editor and two anonymous reviewers for their time and feedbacks.

Appendix A. Supplementary data

Supplementary data to this article can be found online at <https://doi.org/10.1016/j.scitotenv.2023.163745>.

References

- Abatti, B.H., Zanandrea, F., Paul, L.R., Michel, G.P., 2022. Relevance of field data in the assessment of structural and functional sediment connectivity in a small catchment of southern Brazilian plateau. *Earth Surf. Process. Landforms* 1–16. <https://doi.org/10.1002/esp.5507>.
- Alfano, F., Bonadonna, C., Volentik, A.C.M., Connor, C.B., Watt, S.F.L., Pyle, D.M., Connor, L.J., 2011. Tephra stratigraphy and eruptive volume of the May, 2008, Chaitén eruption Chile. *Bull. Volcanol.* 73, 613–630. <https://doi.org/10.1007/s00445-010-0428-x>.

- Arabameri, A., Pradhan, B., Rezaei, K., Lee, C.W., 2019. Assessment of landslide susceptibility using statistical- and artificial intelligence-based FR-RF integrated model and multiresolution DEMs. *Remote Sens.* 11. <https://doi.org/10.3390/rs11090999>.
- Baggio, Tommaso, Martini, Lorenzo, Torresani, Loris, 2022. R_IC.v1.0 (1.0). Zenodo. <https://doi.org/10.5281/zenodo.6566013>.
- Basso-Báez, S., Mazzorana, B., Ulloa, H., Bahamondes, D., Ruiz-Villanueva, V., Iroumé, A., Picco, L., 2020. Unravelling the impacts of the built environment caused by floods in a river heavily perturbed by a volcanic eruption. *J. S. Am. Earth Sci.* 102. <https://doi.org/10.1016/j.jsames.2020.102655>.
- Batalla, R.J., Iroumé, A., Hernández, M., Llena, M., Mazzorana, B., Vericat, D., 2018. Recent geomorphological evolution of a natural river channel in a Mediterranean Chilean basin. *Geomorphology* 303, 322–337. <https://doi.org/10.1016/j.geomorph.2017.12.006>.
- Biass, S., Jenkins, S., Lallemand, D., Lim, T.N., Williams, G., Yun, S.-H., 2021. Remote sensing of volcanic impacts. Forecasting and Planning for Volcanic Hazards, Risks, and Disasters, pp. 473–491. <https://doi.org/10.1016/b978-0-12-818082-2.00012-3>.
- Bracken, L.J., Turnbull, L., Wainwright, J., Bogaart, P., 2015. Sediment connectivity: a framework for understanding sediment transfer at multiple scales. *Earth Surf. Process. Landforms* 40, 177–188. <https://doi.org/10.1002/esp.3635>.
- Bradley, A.P., 1997. The use of the area under the ROC curve in the evaluation of machine learning algorithms. *Pattern Recogn.* 30 (7), 1145–1159. [https://doi.org/10.1016/S0031-3203\(96\)00142-2](https://doi.org/10.1016/S0031-3203(96)00142-2) Available from:.
- Brasington, J., Vericat, D., Rychkov, I., 2012. Modeling River Bed Morphology, Roughness, and Surface Sedimentology Using High Resolution Terrestrial Laser Scanning. 48, pp. 1–18. <https://doi.org/10.1029/2012WR012223>.
- Breiman, L., 2001. Random forests. *Mach. Learn.* 45, 5–31. <https://doi.org/10.1023/A:1010933404324>.
- Casanova, M., Salazar, O., Seguel, O., Luzio, W., 2013. Main features of Chilean soils. The Soils of Chile. World Soils Book Series. Springer, Dordrecht https://doi.org/10.1007/978-94-007-5949-7_2.
- Cavalli, M., Trevisani, S., Comiti, F., Marchi, L., 2013. Geomorphometric assessment of spatial sediment connectivity in small alpine catchments. *Geomorphology* 188, 31–41. <https://doi.org/10.1016/j.geomorph.2012.05.007>.
- Chen, X., Chen, W., 2021. GIS-based landslide susceptibility assessment using optimized hybrid machine learning methods. *Catena* 196. <https://doi.org/10.1016/j.catena.2020.104833>.
- Clapuyt, F., Vanacker, V., Christl, M., Van Oost, K., Schlunegger, F., 2019. Spatio-temporal dynamics of sediment transfer systems in landslide-prone alpine catchments. *Solid Earth* 10, 1489–1503. <https://doi.org/10.5194/se-10-1489-2019>.
- Crisafulli, C.M., Swanson, F.J., Clarkon, B.D., 2015. Volcano ecology: disturbance characteristics and assembly of biological communities. The Encyclopedia of Volcanoes <https://doi.org/10.1016/B978-0-12-385938-9.00073-0>.
- Easdale, M.H., Bruzzzone, O., 2018. Spatial distribution of volcanic ash deposits of 2011 puyehue-Cordón Caulle eruption in Patagonia as measured by a perturbation in NDVI temporal dynamics. *J. Volcanol. Geotherm. Res.* 353, 11–17. <https://doi.org/10.1016/j.jvolgeores.2018.01.020>.
- Embersson, R.A., Kirschbaum, D.B., Stanley, T., 2021. Landslide Hazard and exposure modelling in data-poor regions: the example of the Rohingya refugee camps in Bangladesh. *Earth's Futur.* 9. <https://doi.org/10.1029/2020EF001666>.
- Fryirs, K., 2013. (Dis)Connectivity in catchment sediment cascades: a fresh look at the sediment delivery problem. *Earth Surf. Process. Landforms* 38, 30–46. <https://doi.org/10.1002/esp.3242>.
- Gaidzik, K., Ramírez-Herrera, M.T., 2021. The importance of input data on landslide susceptibility mapping. *Sci. Rep.* 11. <https://doi.org/10.1038/s41598-021-98830-y>.
- Gariano, S.L., Guzzetti, F., 2016. Landslides in a changing climate. *Earth Sci. Rev.* <https://doi.org/10.1016/j.earscirev.2016.08.011>.
- Guzzetti, F., Carrara, A., Cardinali, M., Reichenbach, P., 1999. Landslide hazard evaluation: a review of current techniques and their application in a multi-scale study, Central Italy. *Geomorphology* 31, 181–216. [https://doi.org/10.1016/S0169-555X\(99\)00078-1](https://doi.org/10.1016/S0169-555X(99)00078-1).
- Guzzetti, F., Mondini, A.C., Cardinali, M., Fiorucci, F., Santangelo, M., Chang, K.T., 2012. Landslide inventory maps: new tools for an old problem. *Earth Sci. Rev.* 112, 42–66. <https://doi.org/10.1016/j.earscirev.2012.02.001>.
- Guzzetti, F., Reichenbach, P., Ardizzone, F., Cardinali, M., Galli, M., 2006. Estimating the quality of landslide susceptibility models. *Geomorphology* 81, 166–184. <https://doi.org/10.1016/j.geomorph.2006.04.007>.
- Hassan, M.A., Bird, S., Reid, D., Ferrer-Boix, C., Hogan, D., Brardinoni, F., Chartrand, S., 2019. Variable hillslope-channel coupling and channel characteristics of forested mountain streams in glaciated landscapes. *Earth Surf. Process. Landforms* 44, 736–751. <https://doi.org/10.1002/esp.4527>.
- Heckmann, T., Cavalli, M., Cerdan, O., Foerster, S., Javaux, M., Lode, E., Smetanova, A., Vericat, D., Brardinoni, F., 2018. Indices of sediment connectivity: opportunities, challenges and limitations. *EarthSci. Rev.* <https://doi.org/10.1016/j.earscirev.2018.08.004>.
- Hooke, J., 2003. Coarse sediment connectivity in river channel systems: a conceptual framework and methodology. *Geomorphology* 56, 79–94. [https://doi.org/10.1016/S0169-555X\(03\)00047-3](https://doi.org/10.1016/S0169-555X(03)00047-3).
- Hooke, J., Souza, J., 2021. Challenges of mapping, modelling and quantifying sediment connectivity. *EarthSci. Rev.* <https://doi.org/10.1016/j.earscirev.2021.103847>.
- Iroumé, A., Paredes, A., Garbarino, M., Morresi, D., Batalla, R.J., 2020. Post-eruption morphological evolution and vegetation dynamics of the Blanco River, southern Chile. *J. S. Am. Earth Sci.* 104. <https://doi.org/10.1016/j.jsames.2020.102809>.
- Jones, J.N., Boulton, S.J., Bennett, G.L., Stokes, M., Whitworth, M.R.Z., 2021. Temporal variations in landslide distributions following extreme events: implications for landslide susceptibility modeling. *J. Geophys. Res. Earth Surf.* 126. <https://doi.org/10.1029/2021JF006067>.
- Knoflach, B., Ramskogler, K., Talluto, M., Hofmeister, F., Haas, F., Heckmann, T., Pfeiffer, M., Piermattei, L., Ressler, C., Wimmer, M.H., 2021. Modelling of vegetation dynamics from satellite time series to determine proglacial primary succession in the course of global warming—a case study in the upper Martell Valley (Eastern Italian Alps). *Remote Sens.* 13, 4450.
- Kuhn, M., 2008. Building predictive models in R using the caret package. *J. Stat. Softw.* 28 (5), 1–26. <https://doi.org/10.18637/jss.v028.i05>.
- Korup, O., Seidemann, J., Mohr, C.H., 2019. Increased landslide activity on forested hillslopes following two recent volcanic eruptions in Chile. *Nat. Geosci.* 2–8. <https://doi.org/10.1038/s41561-019-0315-9>.
- Lai, J.S., Tsai, F., 2019. Improving GIS-based landslide susceptibility assessments with multi-temporal remote sensing and machine learning. *Sensors (Switzerland)* 19. <https://doi.org/10.3390/s19173717>.
- Lima, P., Steger, S., Glade, T., Murillo-García, F.G., 2022. Literature review and bibliometric analysis on data-driven assessment of landslide susceptibility. *J. Mt. Sci.* 19, 1670–1698. <https://doi.org/10.1007/s11629-021-7254-9>.
- Lizama, E., Morales, B., Somos-Valenzuela, M., Chen, N., Liu, M., 2022. Understanding landslide susceptibility in northern Chilean Patagonia: a basin-scale study using machine learning and field data. *Remote Sens.* 14. <https://doi.org/10.3390/rs14040907>.
- Lombardo, L., Mai, P.M., 2018. Presenting logistic regression-based landslide susceptibility results. *Eng. Geol.* 244. <https://doi.org/10.1016/j.enggeo.2018.07.019>.
- Lombardo, L., Opitz, T., Ardizzone, F., Guzzetti, F., Huser, R., 2020. Space-time landslide predictive modelling. *EarthSci. Rev.* <https://doi.org/10.1016/j.earscirev.2020.103318>.
- Lucchese, L.V., de Oliveira, G.G., Pedrollo, O.C., 2021. Investigation of the influence of non-occurrence sampling on landslide susceptibility assessment using artificial neural networks. *Catena* 198, 105067. <https://doi.org/10.1016/j.catena.2020.105067>.
- Major, J., Pierson, T.C., Hoblitt, R.P., Moreno, H., 2013. Pyroclastic density currents associated with the 2008–2009 eruption of Chaitén volcano (Chile): Forest disturbances, deposits, and dynamics. *Andean Geol.* 40 (2), 324–358. <https://doi.org/10.5027/andgeoV40n2.a09>.
- Major, J.J., Bertin, D., Pierson, T.C., Amigo, Á., Iroumé, A., Ulloa, H., Castro, J., 2016. Extraordinary sediment delivery and rapid geomorphic response following the 2008–2009 eruption of Chaitén volcano Chile. *Water Resour. Res.* 52, 5075–5094. <https://doi.org/10.1002/2015WR018250>.
- Major, J.J., Mosbrucker, A.R., Spicer, K.R., 2018. Ecological Responses at Mount St. Helens: Revisited a 35 Years After the 1980 Eruption. Springer https://doi.org/10.1007/978-1-4939-7451-1_11.
- Martini, L., Picco, L., Iroumé, A., Cavalli, M., 2019. Sediment connectivity changes in an Andean catchment affected by volcanic eruption. *Sci. Total Environ.* 692, 1209–1222. <https://doi.org/10.1016/j.scitotenv.2019.07.303>.
- Martini, L., Cavalli, M., Picco, L., 2022a. Predicting sediment connectivity in a mountain basin: a quantitative analysis of the index of connectivity. *Earth Surf. Process. Landforms.* <https://doi.org/10.1002/esp.5331>.
- Martini, L., Baggio, T., Torresani, L., Crema, S., Cavalli, M., 2022b. R_IC: a novel and versatile implementation of the index of connectivity in R. *Environ. Model. Softw.* 155. <https://doi.org/10.1016/j.envsoft.2022.105446>.
- Maxwell, A.E., Shobe, C.M., 2022. Land-surface parameters for spatial predictive mapping and modeling. *EarthSci. Rev.* <https://doi.org/10.1016/j.earscirev.2022.103944>.
- Michellini, T., Bettella, F., D'Agostino, V., 2017. Field investigations of the interaction between debris flows and forest vegetation in two alpine fans. *Geomorphology* 279, 150–164. <https://doi.org/10.1016/j.geomorph.2016.09.029>.
- Minár, J., Evans, I.S., Jenčo, M., 2020. A comprehensive system of definitions of land surface (topographic) curvatures, with implications for their application in geoscientific modelling and prediction. *EarthSci. Rev.* <https://doi.org/10.1016/j.earscirev.2020.103414>.
- Meyer, H., Milà, C., Ludwig, M., 2023. CAST: 'caret' applications for spatial-temporal models. <https://github.com/HannaMeyer/CAST> <https://hannameyer.github.io/CAST/>.
- Morales, B., García-Pedrero, A., Lizama, E., Lillo-Saavedra, M., Gonzalo-Martín, C., Chen, N., Somos-Valenzuela, M., 2022. Patagonian Andes landslides inventory: the deep learning's way to their automatic detection. *Remote Sens.* <https://doi.org/10.3390/rs14184622>.
- Morales, B., Lizama, E., Somos-Valenzuela, M.A., Lillo-Saavedra, M., Chen, N., Fustos, I., 2021. A comparative machine learning approach to identify landslide triggering factors in northern Chilean Patagonia. *Landslides* 18, 2767–2784. <https://doi.org/10.1007/s10346-021-01675-9>.
- Murgia, I., Giadrossich, F., Mao, Z., Cohen, D., Capra, G.F., Schwarz, M., 2022. Modeling shallow landslides and root reinforcement: a review. *Ecol. Eng.* 181. <https://doi.org/10.1016/j.ecoleng.2022.106671>.
- Ortiz-Rodríguez, A.J., Borselli, L., Sarocchi, D., 2017. Flow connectivity in active volcanic areas: use of index of connectivity in the assessment of lateral flow contribution to main streams. *Catena* 157, 90–111. <https://doi.org/10.1016/j.catena.2017.05.009>.
- Ortiz-Rodríguez, A.J., Capra, L., Muñoz-Robles, C., Coviello, V., Borselli, L., 2020. Connectivity and hydrological efficiency dynamics at active volcanoes, Mexico. *Sci. Total Environ.* 736, 139649. <https://doi.org/10.1016/j.scitotenv.2020.139649>.
- Parra, E., Mohr, C.H., Korup, O., 2021. Predicting patagonian landslides: roles of Forest cover and wind speed. *Geophys. Res. Lett.* <https://doi.org/10.1029/2021GL095224>.
- Pellegrini, G., Martini, L., Cavalli, M., Rainato, R., Cazorzi, A., Picco, L., 2021. The morphological response of the Tegnás alpine catchment (Northeast Italy) to a large infrequent disturbance. *Sci. Total Environ.* 770, 145209. <https://doi.org/10.1016/j.scitotenv.2021.145209>.
- Picco, L., Comiti, F., Mao, L., Tonon, A., Lenzi, M.A., 2017. Medium and short term riparian vegetation, island and channel evolution in response to human pressure in a regulated gravel bed river (Piave River, Italy). *Catena* 149, 760–769. <https://doi.org/10.1016/j.catena.2016.04.005>.
- Pierson, T.C., Major, J.J., Amigo, Á., Moreno, H., 2013. Acute sedimentation response to rainfall following the explosive phase of the 2008–2009 eruption of Chaitén volcano Chile. *Bull. Volcanol.* 75, 1–17. <https://doi.org/10.1007/s00445-013-0723-4>.
- Poeppl, R.E., Fryirs, K.A., Tunncliffe, J., Brierley, G.J., 2020. Managing sediment (dis)connectivity in fluvial systems. *Sci. Total Environ.* 736. <https://doi.org/10.1016/j.scitotenv.2020.139627>.

- Pourghasemi, H.R., Kornejady, A., Kerle, N., Shabani, F., 2020. Investigating the effects of different landslide positioning techniques, landslide partitioning approaches, and presence-absence balances on landslide susceptibility mapping. *Catena* 187. <https://doi.org/10.1016/j.catena.2019.104364>.
- Rabby, Y.W., Li, Y., 2020. Landslide susceptibility mapping using integrated methods: a case study in the Chittagong hilly areas, Bangladesh. *Geoscience* 10, 1–26. <https://doi.org/10.3390/geosciences10120483>.
- Rathburn, S.L., Bennett, G.L., Wohl, E.E., Briles, C., McElroy, B., Sutfin, N., 2017. The fate of sediment, wood, and organic carbon eroded during an extreme flood, Colorado front range, USA. *Geology* 45, 499–502. <https://doi.org/10.1130/G38935.1>.
- Regmi, N.R., Giardino, J.R., McDonald, E.V., Vitek, J.D., 2014. A comparison of logistic regression-based models of susceptibility to landslides in western Colorado, USA. *Landslides* 11, 247–262. <https://doi.org/10.1007/s10346-012-0380-2>.
- Reichenbach, P., Rossi, M., Malamud, B.D., Mihir, M., Guzzetti, F., 2018. A review of statistically-based landslide susceptibility models. *EarthSci. Rev.* <https://doi.org/10.1016/j.earscirev.2018.03.001>.
- Roy, P., Ghosal, K., Paul, P.K., 2022. Landslide susceptibility mapping of Kalimpong in Eastern Himalayan Region using a Rprop ANN approach. *Earth Syst* 131, 130.
- Saito, H., Uchiyama, S., Teshirogi, K., 2022. Rapid vegetation recovery at landslide scars detected by multitemporal high-resolution satellite imagery at Aso volcano Japan. *Geomorphology* 398, 107989. <https://doi.org/10.1016/j.geomorph.2021.107989>.
- Sanchis-Ibor, C., Segura-Beltrán, F., Almonacid-Caballer, J., 2017. Channel forms recovery in an ephemeral river after gravel mining (Palancia River, eastern Spain). *Catena* 158, 357–370. <https://doi.org/10.1016/j.catena.2017.07.012>.
- Schopper, N., Mergili, M., Frigerio, S., Cavalli, M., Poepl, R., 2019. Analysis of lateral sediment connectivity and its connection to debris flow intensity patterns at different return periods in the Fella River system in northeastern Italy. *Sci. Total Environ.* 658, 1586–1600. <https://doi.org/10.1016/j.scitotenv.2018.12.288>.
- Skeffington, M.S., Hall, K., 2011. The ecology, distribution and invasiveness of *Gunnera L.* species in Connemara, Western Ireland. *Biol. Environ.* 111, 1–19. <https://doi.org/10.3318/BIOE.2011.13>.
- Somos-Valenzuela, M.A., Oyarzun-Ulloa, J.E., Fustos-Toribio, I.J., Garrido-Urzu, N., Chen, N., 2020. The mudflow disaster at villa Santa Lucía in Chilean Patagonia: understandings and insights derived from numerical simulation and postevent field surveys. *Nat. Hazards Earth Syst. Sci.* 20, 2319–2333. <https://doi.org/10.5194/nhess-20-2319-2020>.
- Spiekermann, R.I., Smith, H.G., McColl, S., Burkitt, L., Fuller, I.C., 2022a. Development of a morphometric connectivity model to mitigate sediment derived from storm-driven shallow landslides. *Ecol. Eng.* 180. <https://doi.org/10.1016/j.ecoleng.2022.106676>.
- Spiekermann, R.I., Smith, H.G., McColl, S., Burkitt, L., Fuller, I.C., 2022b. Quantifying effectiveness of trees for landslide erosion control. *Geomorphology* 396. <https://doi.org/10.1016/j.geomorph.2021.107993>.
- Steger, S., Scorpio, V., Comiti, F., Cavalli, M., 2022. Data-driven modelling of joint debris flow release susceptibility and connectivity. *Earth Surf. Process. Landforms.* <https://doi.org/10.1002/esp.5421>.
- Sulaiman, M.S., Goh, Q.Y., Sang, Y.F., Sivakumar, B., Ali, A., Rasit, N., Abood, M.M., 2021. Development of river morphologic stability index (RMSI) to assess mountain river systems. *J. Hydrol. Reg. Stud.* 37. <https://doi.org/10.1016/j.ejrh.2021.100918>.
- Sun, D., Wen, H., Wang, D., Xu, J., 2020. A random forest model of landslide susceptibility mapping based on hyperparameter optimization using bayes algorithm. *Geomorphology* 362, 107201. <https://doi.org/10.1016/j.geomorph.2020.107201>.
- Swanson, F.J., Jones, J.A., Crisafulli, C.M., Lara, A., 2013. Effects of volcanic and hydrologic processes on forest vegetation : Chaitén volcano Chile. *Andean Geol.* 40, 359–391. <https://doi.org/10.5027/andgeoV40n2-a10>.
- Tanyu, B.F., Abbaspour, A., Alimohammadlou, Y., Tecuci, G., 2021. Landslide susceptibility analyses using random Forest, C4.5, and C5.0 with balanced and unbalanced datasets. *Catena* 203. <https://doi.org/10.1016/j.catena.2021.105355>.
- Teltscher, K., Fassnacht, F.E., 2018. Using multispectral landsat and Sentinel-2 satellite data to investigate vegetation change at Mount St. Helens since the great volcanic eruption in 1980. *J. Mt. Sci.* 15, 1851–1867. <https://doi.org/10.1007/s11629-018-4869-6>.
- Tonon, A., Iroumé, A., Picco, L., Oss-Cazzador, D., Lenzi, M.A., 2018. Temporal variations of large wood abundance and mobility in the Blanco River affected by the Chaitén volcanic eruption, southern Chile. *Catena* 156, 149–160. <https://doi.org/10.1016/j.catena.2017.03.025>.
- Trigila, A., Iadanza, C., Esposito, C., Scarascia-Mugnozza, G., 2015. Comparison of logistic regression and random forests techniques for shallow landslide susceptibility assessment in giampilieri (NE Sicily, Italy). *Geomorphology* 249, 119–136. <https://doi.org/10.1016/j.geomorph.2015.06.001>.
- Tsunetaka, H., Asano, S., Murakami, W., 2022. Do standing trees affect landslide mobility on forested hillslopes in Japan? *Earth Surf. Process. Landforms.* <https://doi.org/10.1002/esp.5461>.
- Ulloa, H., Iroumé, A., Picco, L., Mohr, C.H., Mazzorana, B., Lenzi, M.A., Mao, L., 2016. Spatial analysis of the impacts of the Chaitén volcano eruption (Chile) in three fluvial systems. *J. S. Am. Earth Sci.* 69, 213–225. <https://doi.org/10.1016/j.jsames.2016.04.008>.
- Ulloa, H., Mazzorana, B., Batalla, R.J., Julian, C., Iribarren-Anacona, P., Barrientos, G., Reid, B., Oyarzun, C., Schaefer, M., Iroumé, A., 2018. Morphological characterization of a highly-dynamic fluvial landscape: the river baker (Chilean Patagonia). *J. S. Am. Earth Sci.* 86, 1–14. <https://doi.org/10.1016/j.jsames.2018.06.002>.
- Villablanca, L., Batalla, R.J., Piqué, G., Iroumé, A., 2022. Hydrological effects of large dams in Chilean rivers. *J. Hydrol. Reg. Stud.* 41. <https://doi.org/10.1016/j.ejrh.2022.101060>.
- Wang, W., Godard, V., Liu-Zeng, J., Scherler, D., Xu, C., Zhang, J., Xie, K., Bellier, O., Ansberque, C., de Sigoyer, J., 2017. Perturbation of fluvial sediment fluxes following the 2008 wenchuan earthquake. *Earth Surf. Process. Landforms* 42, 2611–2622. <https://doi.org/10.1002/esp.4210>.
- Wasko, C., Nathan, R., Peel, M.C., 2020. Trends in global flood and streamflow timing based on local water year. *Water Resour. Res.* 56, 1–12. <https://doi.org/10.1029/2020WR027233>.
- Wilson, R., Harrison, S., Reynolds, J., Hubbard, A., Glasser, N.F., Wüdrich, O., Iribarren Anaconda, P., Mao, L., Shannon, S., 2019. The 2015 Chileno Valley glacial lake outburst flood, Patagonia. *Geomorphology* 332, 51–65. <https://doi.org/10.1016/j.geomorph.2019.01.015>.
- Wohl, E., Brierley, G., Cadol, D., Coulthard, T.J., Covino, T., Fryirs, K.A., Sklar, L.S., 2018. Connectivity as an emergent property of geomorphic systems. *Earth Surf. Process. Landf.* <https://doi.org/10.1002/esp.4434>.
- Wu, Z., Baartman, J.E.M., Pedro Nunes, J., López-Vicente, M., 2023. Intra-annual sediment dynamic assessment in the Wei River basin, China, using the AIC functional-structural connectivity index. *Ecol. Indic.* 146. <https://doi.org/10.1016/j.ecolind.2022.109775>.
- Yi, Y., Zhang, Z., Zhang, W., Jia, H., Zhang, J., 2020. Landslide susceptibility mapping using multiscale sampling strategy and convolutional neural network: a case study in jiuzaigou region. *Catena* 195. <https://doi.org/10.1016/j.catena.2020.104851>.
- Zanandrea, F., Michel, G.P., Kobiyama, M., 2020. Impedance influence on the index of sediment connectivity in a forested mountainous catchment. *Geomorphology* 351. <https://doi.org/10.1016/j.geomorph.2019.106962>.